Heliyon 8 (2022) e10032

Contents lists available at ScienceDirect

Heliyon

journal homepage: www.cell.com/heliyon

Research article

Semiconductor to metallic transition in double halide perovskites $Cs_2AgBiCl_6$ through induced pressure: A DFT simulation for optoelectronic and photovoltaic applications

Md. Nurul Islam, Jiban Podder *

Department of Physics, Bangladesh University of Engineering and Technology, Dhaka-1000, Bangladesh

ARTICLE INFO

Keywords:
$Cs_2AgBiCl_6$
Phase stability
Mechanical
Optical
Electronic properties
Photocatalyst

ABSTRACT

Double halide perovskites ($A_2M^+M^{3+}_3X_6$) have been considered as high-performance material for optoelectronic and photovoltaic devices. Here, we investigate the structural, thermodynamic, optical, mechanical and electronic properties of pressure-induced $Cs_2AgBiCl_6$ samples. The phase stability is confirmed by the tolerance and octahedral factor calculations. The thermodynamic potentials such as enthalpy, free energy, entropy, and heat capacity are observed in the phonon modes. The indirect to direct band gap is observed due to disorders of Ag^+/Bi^{3+} cations in their sub-lattice. In this study, the induced pressure was varied between 0 and 80 GPa and the transition of the band gap energy from semiconductor to metal was observed at a hydrostatic pressure of 80 GPa. The bond length in between Ag and Bi atoms is reduced due to crystal defect, occurred under induced pressure. The narrow band gap energy and the partial density of states of the disordered $Cs_2AgBiCl_6$ samples refer to the relocation of charge carriers to facilitate the photocatalytic reaction. As the pressure changes, the absorbing edge also moves into the lower energy region. The pressure-inducted $Cs_2AgBiCl_6$ sample has a strong absorption in the range of visible wavelength of light and shifted in the ultraviolet region. Simultaneously, the pressure-driven material extend the symmetry breaking of $[AgBi]^{-6}$ and $[AgCl]^{-6}$ octahedra and hence the total energy decreased due to narrow band gap energy. Phase-change dihalide materials have excellent properties, opening up new avenues for device applications. The mechanical properties suggest that the pure and pressure-inducted $Cs_2AgBiCl_6$ samples have potential characteristics for an optoelectronic and photovoltaic applications.

1. Introduction

Recently, double halide perovskites are recognized as promising candidates for photovoltaic and optoelectronic devices owing to their excellent phase, thermal, structural, electrical, optical, and dynamic stability [1, 2, 3, 4, 5]. Many researchers report that $Cs_2AgBiCl_6$ halide perovskites have been used in solar cells, lasers, light-emitting diodes (LEDs) and radiation detection. Lead-based hybrid halide perovskites have excellent photovoltaic properties, despite the long-term negative impact on the environment [6]. Over the past few decades, researchers have attempted to find bimetallic halides for cost effective optoelectronic devices to transcend the limitations of instability and toxicity.

The standard chemical formula for metal halides is $A_2M^+M^{3+}_3X_6$, where, A = earth metal, M^+ = monovalent, M^{3+} = trivalent, X = halide [7]. Recently, double halide perovskites have found potential applications in optoelectronic devices [8, 9]. Due to easy ion's transition in monovalent and trivalent cations, Bi-based organic and inorganic double metal halides are used in a solar cell device. Non-toxic double halide $Cs_2AgBiCl_6$ has indirect band gap energy of 1.83 eV and the sub-lattice disorder of Ag and Bi has a great influence on the energy band gap [10]. Disordered (Ag, Bi) anti-site defects occur within the $Cs_2AgBiCl_6$ lattice network due to the transferred direct band gap of 0.62 eV. Here, we used driving pressure on the $Cs_2AgBiCl_6$ lattice network. Among the disordered Ag and Bi atoms in the $Cs_2AgBiCl_6$, the Ag-3d and Bi-6p orbital electrons are hybridized due to the reduced band gap.

Recently, theoretically based DFT simulations of $Cs_2AgBiCl_6$ [11] reported that an indirect transfer of the band gap to direct can occur via Sn^{2+} (Ge^{2+}) doping. Due to Sn and Ge doping, the light absorption changes significantly and the exciton binding energy is significantly reduced. The valence band maximum (VBM) and conduction band minimum (CBM) of the pure $Cs_2AgBiCl_6$ sample are located at multiple k-points in the Brillouin zone, demonstrating indirect band gap

* Corresponding author.
E-mail address: jpodder59@gmail.com (J. Podder).

https://doi.org/10.1016/j.heliyon.2022.e10032
Received 4 January 2022; Received in revised form 25 March 2022; Accepted 18 July 2022

properties. This fact is especially important for comprehending the pressure depends on the distribution of space charge at various k-points energies.

The properties of semiconductor material can easily tune by applying a hydrostatic pressure [12, 13, 14]. L. Wang et al. noted the structural phase change of lead halide perovskite $CH(NH_2)_2PbBr_3$ at a pressure of 2.2 GPa [15]. The pressure-driven $Cs_2AgBiCl_6$ sample decreases the energy of the band gap and oriented the electron orbits towards the electric field. As the outcome, the bond energy of the octahedral state changes, affecting the boundary conditions of the electron wave function, thereby reducing the band gap energy. We find that under driving pressure, the absorption peaks shift to the red-shifted- region owing to distortion inside the $[AgBr6]^{5-}$ and $[BiBr6]^{3-}$octahedral states.

In this study, we investigated the indirect to the direct band gap transition in $Cs_2AgBiCl_6$ through the disordered Ag^{+}/Bi^{3+} cations in their sub-lattices and also search semiconductors to metals by inducing hydrostatic pressure. Hence, this study will provide a better understanding of double halide perovskites on tunability of the electronic band gap and metallization. Furthermore, we investigate uncompressed and compressed structural, mechanical, optical, electronic and photocatalytic properties of $Cs_2AgBiCl_6$ double halide perovskites applying the Density Functional Theory (DFT). We anticipate that $Cs_2AgBiCl_6$ would be a favorable candidate for the applications in optoelectronic and photovoltaic devices.

2. Theoretical methodology

DFT was carried out applying plane-wave-based CASTEP Code material studio, 2017 package [16, 17]. The exchange correlation potential energy and the projected enhancement wave (PAW) pseudopotential are described using the non-spin polarized Perdew-Burke-Ernzerhof (PBE) function in the general gradient approximation (GGA) method [18, 19, 20]. We applied 4 × 4 × 4 gamma centered (Γ) k-points to pure and pressure-induced $Cs_2AgBiCl_6$. $5s^2\ 5p^6\ 6s^1$ for Cs, 4d10 $5s^1$ for Ag, $6s^2\ 6p^3$ for Bi, and $3s^2\ 3p^5$ for Cl, the electron configuration is done in the valence band based on the partial density of states (PDOS) calculations. In this work, the unit cell of $Cs_2AgBiCl_6$ is used for all calculations in a 1 × 1×1 super-cell model. The results of plane wave cutoff energy convergence for structural optimization are shown in Figure 1. An energy cutoff of 420 eV was found to be sufficient to achieve converged ground state energy for $Cs_2AgBiCl_6$. Hence, the cutoff energy 420 eV was applied for uncompressed and compressed $Cs_2AgBiCl_6$.

To see the absorption and dielectric spectra, a value of 0.25 eV was applied instead of the theoretical and experimental band gap energy of the double halide $Cs_2AgBiCl_6$ 1.91 eV and 2.16 eV, respectively [21, 22]. Both pure and pressure-driven Cs2AgBiCl6 are maximized by decreasing the total energy, internal force, and external stress using the Broyden-Fletcher-Goldfarb-Shanno (BFGS) algorithm with change of constant lattice parameters and internal coordinates. The unit cell structure and atomic relaxation of $Cs_2AgBiCl_6$ have been accomplished under the residual forces 0.03 eV/Å. To calculate the elastic modulus C_{ij}, the finite strain theory was applied [16, 23, 24]. The stress tensor has six independent stress parameters σij, and each strain δj corresponds to a unit cell. Finite displacement super-cell technology is used to calculate lattice dynamics such as phonon dispersion.

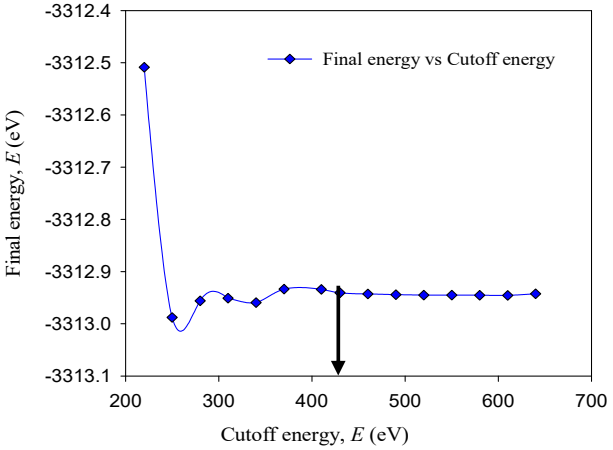

Figure 1. Plane-wave cutoff energy convergences for structural optimize.

3. Results and discussion

3.1. Structural parameters and phase stability

The metal halide $Cs_2AgBiCl_6$ perovskite is a cubic-structure having space group $Fm\bar{3}m$ (No. 225). Hence, Cs atoms are occupied at face centered position with 8c Wyckoff site and fractional coordinates (0.25 0.25 0.25), Bi atoms are positioned at the body-centered with 4b Wyckoff site and fractional coordinates (0.5 0.5 0.5), Ag atoms are situated at corner position with 4a Wyckoff site and fractional coordinate (0 0 0), and Cl atoms are situated at a face-centered position in the unit cell with 24e Wyckoff sites and fractional coordinates (0.2513 0 0). The visualization of the 1 × 1×1 super-cell ordered and disordered structures of the $Cs_2AgBiCl_6$ are displayed in Figure 2. The simulated structural parameters, *a* match well with previously published manuscripts, as shown in Table 1. Two Cs^{+}, one Bi^{3+}, one Ag^{+} and six Cl ions coupled to adjacent Bi^{3+} and Ag^{+} ions form the unit cell of $Cs_2AgBiCl_6$. Ag/Bi disordered samples have a slightly different lattice parameter, a (10.86 Å) and cell volume V (1325 $Å^3$) from the $Cs_2AgBiCl_6$ order due to the mismatch of Ag^{+} (0.89 Å) and Bi^{3+} (3.36 Å) ions. The DFT-based simulated structural parameters were found to be closer to the experimental manuscript [25].

As expected, the unit cell parameters decrease under compression. As a result, the repulsion becomes more powerful in between the atoms, changing the hardness of the sample compression under applied pressure. The material should have phase stability to be used for precise device applications. First, the material must have a fully filled elastic modulus condition to achieve mechanical stability. The stability of the phase tolerance is measured using Eq. (1) [26].

$$t = (R_A + R_X)/\sqrt{2}\ [(R_{B/} + R_{B//})/2 + R_X]. \quad (1)$$

The octahedral factor is given by Eq. (2).

$$\mu = (R_{B/} + R_{B//})\ /\ 2R_X \quad (2)$$

In order to calculate the stability, the tolerance and octahedral factor are to be in the range $0.81 < t < 1.0$ and $0.81 < \mu < 1.0$. In order to find the phase stability, Shannon ion radius was used. For $Cs_2AgBiCl_6$ the calculated, $\mu = 0.41$ and $t = 0.92$ depicts that the sample belongs to standard halide perovskites.

3.1.1. Dynamic and thermodynamic stability

In order to obtain stable natural gain, the sample must meet some special requirements. To observe the dynamic properties, we employ the finite displacement method by analyzing the phonon dispersion curve. The crystal lattice must be constant for dynamic stability. Second, there would not be the sifting of phonon modes in the graph of the phonon dispersion. Soft phonon mode refers to the movement of a group of atoms from a structure of high crystal symmetry to a structure of low crystal symmetry indicates that the sample is unstable. Soft mode, phonon dispersion contains imaginary mode frequency (negative). The phonon dispersion graphs are shown in Figure 3 (a). The phonon frequency must have positive values in a dynamic stable crystal. Notably, imaginary frequencies are not maintained at points W, L, K, Γ and X, indicating a stable mode.

To observe the thermodynamic stability, we calculated the phonon properties. We calculated the thermodynamic potentials viz. enthalpy (H), the free energy (F), and the entropy (S) at the constant temperature

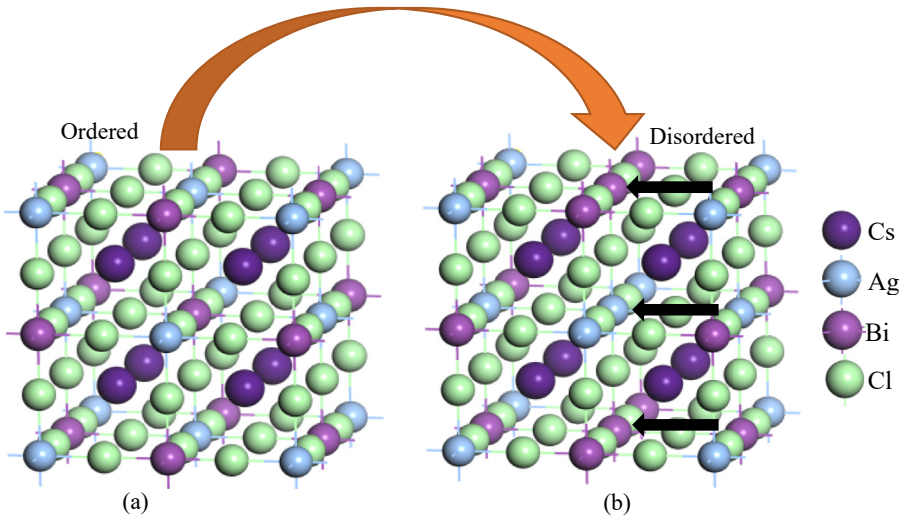

Figure 2. 1×1×1 super cell (a) ordered and (b) disordered structure of $Cs_2AgBiCl_6$.

Table 1. The simulated lattice parameter *a* compared with the previously published manuscript.

a (Å)			
Pressure (GPa)	Present study	Simulation	Experimental
0	11.11	10.92 [25]	10.77 [25],10.78 [11]
20	9.81	-	-
40	9.35	-	-
50	9.19	-	-
60	9.06	-	-
70	8.93	-	-
80	8.84	-	-

with the help of phonon properties. The involvement of vibrations to enthalpy, free energy and entropy are represented by eqn. no. (3), (4) and (5), respectively [27].

$$H(\mathrm{T}) = \mathrm{E_{tot}} + \frac{1}{2}\int \mathrm{g}(\omega)\hbar\omega \mathrm{d}\omega + \int \frac{\hbar\omega}{\mathrm{e}^{\frac{\hbar\omega}{\mathrm{k_B T}}} - 1}\mathrm{g}(\omega)\mathrm{d}\omega \tag{3}$$

$$F(T) = E_{tot} + \frac{1}{2}\int g(\omega)\hbar\omega d\omega + k_B T \int g(\omega)\ln\left(1 - e^{\frac{\hbar\omega}{k_B T}}\right)d\omega \tag{4}$$

$$S(T) = k_B\left[\int \frac{\frac{\hbar\omega}{k_B T}}{e^{\frac{\hbar\omega}{k_B T}} - 1} g(\omega)d\omega - \int g(\omega)\ln\left(1 - e^{\frac{\hbar\omega}{k_B T}}\right)d\omega\right] \tag{5}$$

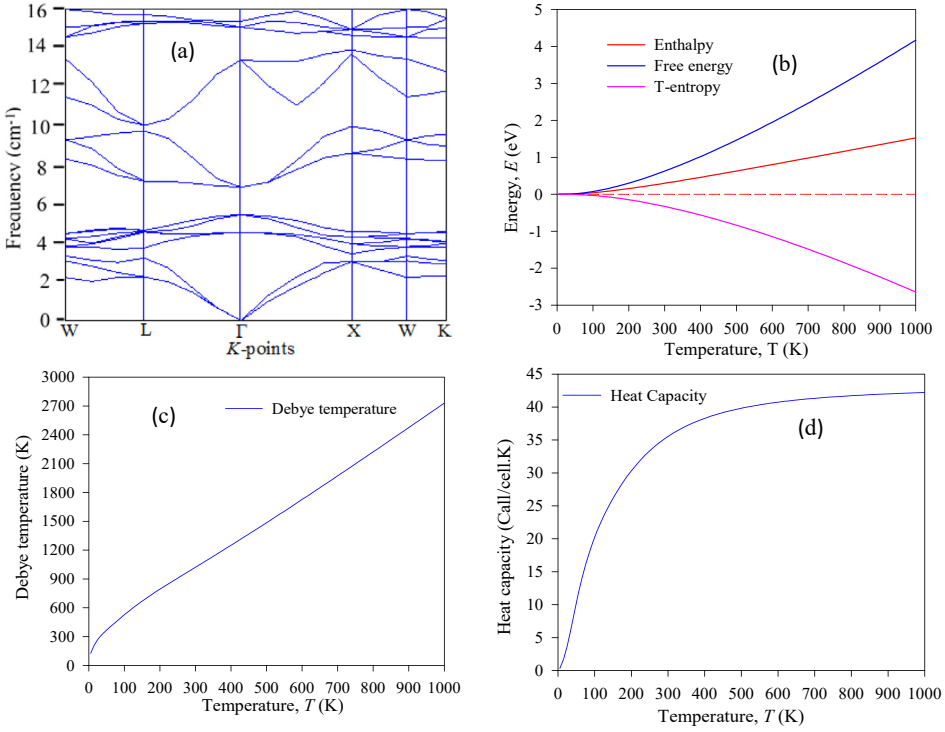

Figure 3. (a) Phonon dispersion curves high symmetry direction, (b) thermodynamic properties, (c) Debye temperature and (d) heat capacity of 80 GPa for $Cs_2AgBiCl_6$.

Herein, g (ω) represents the states of phonon density and k_B is the Boltzmann constant.

Figure 3(b-d) refers to the temperature dependence of simulated thermodynamic properties belonging to the pressure-induced enthalpy, free energy and entropy of $Cs_2AgBiCl_6$. Hence, the enthalpy and the free energy are increased by varying temperatures, whereas, entropy is decreased by varying temperatures. Figure 3 (b-d) also depicts that the three thermodynamic potentials (H, F and S) become zero as the temperature goes to zero. This phenomenon is in good agreement with the third law of thermodynamics. Remarkably, the thermal capacity addresses the Dulong-Petit limit at high temperature. Based on the thermodynamic properties, we predict that pure and pressure-induced $Cs_2AgBiCl_6$ are thermodynamically stable in nature.

3.2. Electronic properties

In viewing the electronic properties of ordered and disordered cubic hybrid perovskites $Cs_2AgBiCl_6$, we study the electron band energies along the high symmetry points. We applied hydrostatic pressure to the metallization in the estimated $Cs_2AgBiCl_6$ compound. Figure 4(a-d) shows the simulated electronic band structure. The HSC (Heyd-Scuseria-Ernzerhof) method is suitable for accurate band gap measurements [28]. However, our main goal is to see metallization, since the band gap error of the general gradient approximation (GGA) method is ignored. Figure 4(a) shows that the k-points in the valence and conduction bands are different and the ordered samples show indirect band gap. The pure $Cs_2AgBiCl_6$ has strong absorption, long charge carrier lifetime and the indirect band gap nature. The indirect belongs to the high potential applications of the samples in photovoltaic devices. In the indirect band gap, the electrons move from the highest energy level of the valence band to the minimum energy level of the conduction band with different momentum energy. The indirect band energies are converted to direct band energies through the disordering of Ag^+/Bi^{3+} cations in the sub-lattice.

Meanwhile, the disorder of Ag^+/Bi^{3+} cations in its sub-lattice increases the symmetry breaking of the $[AgBi]^{-6}$ and $[AgCl]^{-6}$ octahedra, thereby reducing the electronic band gap energy. Figure 4 (a) shows that the conduction band (CB) minimum and valence band (VB) maximum falls at R→Γ, indicating the existence of an indirect band gap in ordered $Cs_2AgBiCl_6$. But in disordered $Cs_2AgBiCl_6$, the CB minimum and VB maximum are located at k-point Γ, indicating a direct band gap nature. The band energy is shifted to a lower energy, i.e., 'red-shift' in disordered samples compared to ordered samples. In general, semiconductors of indirect nature are promising candidates for photovoltaic, while direct band gap samples are applications for optoelectronic devices [29].

The simulated energy band gap is found in good fitting with the published theoretical and experimental results [28, 30, 31]. Due to the orbital motion towards the electric field, the electronic band gap decreases with pressure and eventually experiences the metallic band gap. The total density of states (TDOS) and the partial density of states (PDOS) of ordered and disordered $Cs_2AgBiCl_6$ double halide perovskites are shown in Figures 5 (a-d). As shown in the images of TDOS and PDOS, the VB is mostly Ag-4d and Bi-5d orbits with small contributions of Cs-6s and Cl-3p states. The high energy band has little contributions from Cs-6s and Cl-3p orbitals. The TDOS of disordered $Cs_2AgBiCl_6$ becomes wider than that of ordered $Cs_2AgBiCl_6$, specifies that the higher order electron delocalization due to the loss of crystal symmetry.

3.2.1. Analysis of Mulliken population and charge density distribution

Mulliken population analysis gives information on the charge, bond length and bond population in a solid crystalline sample, which helps to determine the distribution of charge in forming the bonds [31, 32]. Mulliken effective charge is determined by the eqn. no. (6) [32]

$$Q(\alpha) = \sum_k W_k \sum_{\mu}^{on\ \alpha} \sum_{\mu} P_{\mu\nu}(k) S_{\mu\nu}(k) \tag{6}$$

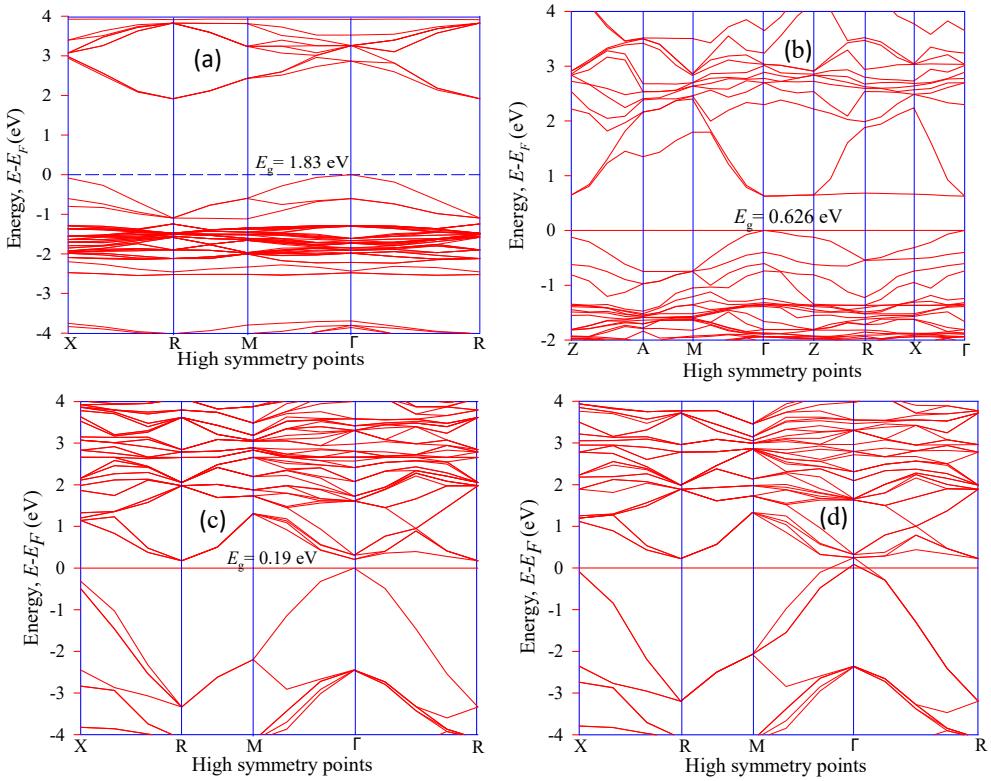

Figure 4. The electronic band structure of (a) pure, (b) disordered, (c) pressure induced at 70 GPa and (d) pressure induced at 80 GPa of $Cs_2AgBiCl_6$.

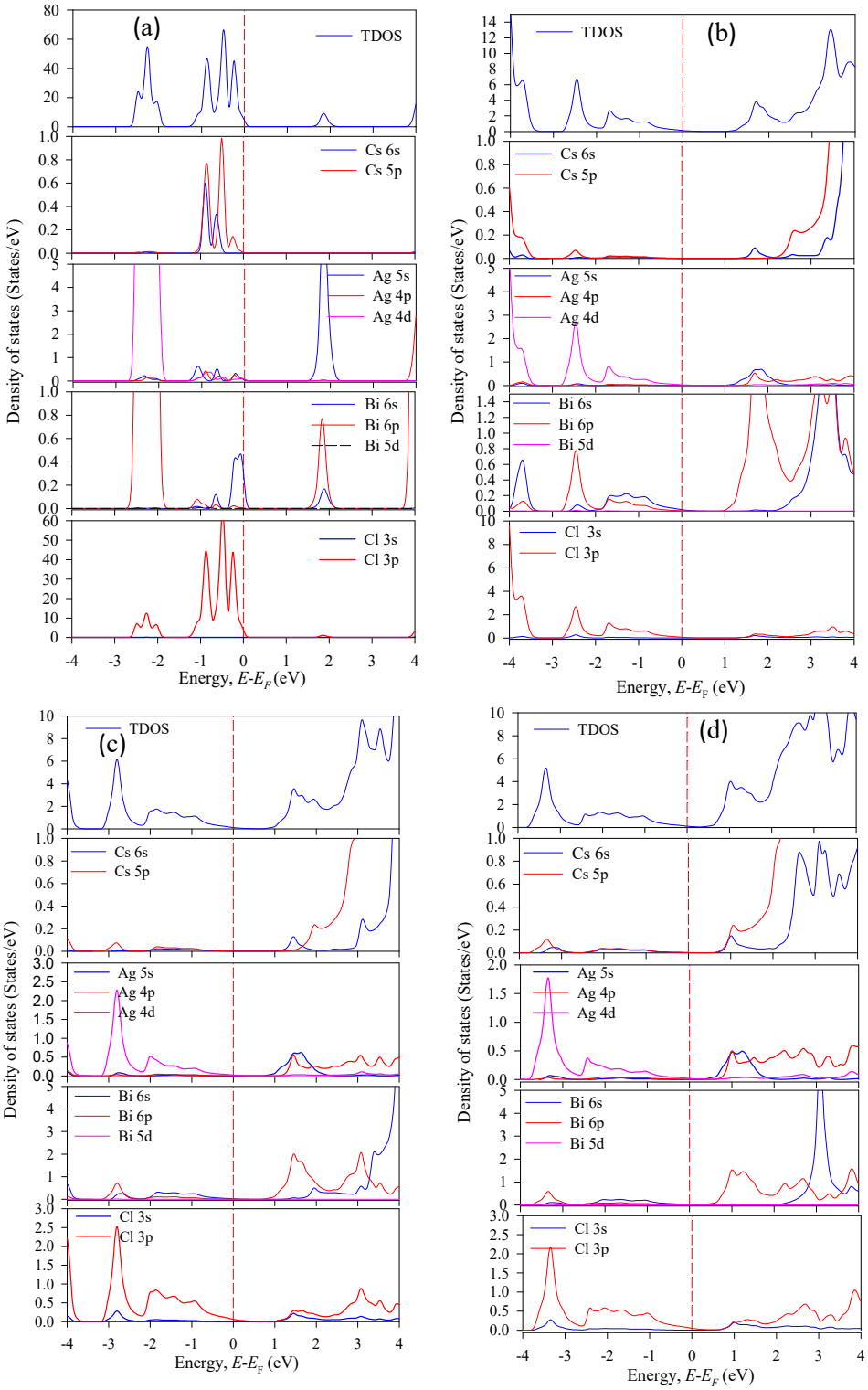

Figure 5. The total and partial density of states (a) pure, (b) disordered, (c) pressure induced at 70 GPa and (d) pressure induced at 80 GPa of $Cs_2AgBiCl_6$.

Here, $P_{\mu\nu}$ refers the density matrix of an element and $S_{\mu\nu}$ (k) represents the overlap matrix.

The overlaped population is occurred within two atoms, $\alpha\beta$ can be expressed by the following Eq. (7) [32]

$$(p(\alpha\beta)) = \sum_k W_k \sum_{on\ \alpha}^{on\ \alpha} \sum_{\nu}^{on\ \beta} 2P_{\mu\nu}(k)S_{\mu\nu}(k) \tag{7}$$

Notably, the Mulliken effective charge of the spacer Cs, Ag, Bi, and Cl atoms were found to be smaller than their ionic charges, viz. $^{+}1$, $^{+}2$, $^{+}3$, and $^{-}1$, respectively. To separate the Milliken effective charge and the ionic radius, Shannon ionic radius was used. Mulliken effective charge and formal ionic radius values estimate the blend of ionic and covalent bonds.

Mulliken effective charges (e) are varying at different driven hydrostatic pressure. It is seen that the Mulliken effective charge (e) does not

follow any trend due to the variant form ionic radius of Ag atoms. A positive number of bonds indicate a high degree of covalentity; conversely, a small group of bonds refers to a high degree of similarity in covalent bonds [33, 34]. From Table 2, we observe that the pressure-driven Cl–Ag and Cl–Bi bond lengths decrease at different induced pressures due to the binding of ionic radii to each other. The shift in inter-octahedral Cl–Ag and Cl–Bi bond lengths is caused for the crystal defect that occurred in Ag and Bi atoms. The intra-octahedral bonds (Cl–Ag and Cl–Bi) are relatively stronger in compared to pressure induced samples due to van der Waals force of the former Cl–Ag and Cl–Bi bonds. Under the induced pressure at 80 GPa, Ag and Bi atoms formed a weak bond. Simultaneously, symmetry breaking occurs within the $[AgBr6]^{5-}$ and $[BiBr6]^{3-}$octahedral sites when the induced pressure experiences 0 GPa–80 GPa.

The bond length of Cl–Ag is 2.80 Å in the ordered $Cs_2AgBiCl_6$, which decreases to 2.65 Å when the structure transitions to a disordered structure. Likewise, the bond length of Bi–Cl in $Cs_2AgBiCl_6$ decreases from 2.75 Å to 2.65 Å when the system is transformed from an ordered system to a disordered one. Finally, the lower bond length is found when the band gap energy undergoes indirect to direct. For the pressure-induced samples, the Ag–Br bond length was reduced and the $Cs_2AgBiCl_6$ sample was transformed from semiconductors to metals. It gives an idea about the bonding properties through charge density (e/Å^3) of pure and pressure-induced distribution of $Cs_2AgBiCl_6$. Figure 6 shows the estimated charge density of the $Cs_2AgBiCl_6$ sample. We have seen that the charge densities of the pure $Cs_2AgBiCl_6$ sample and the pressure-driven $Cs_2AgBiCl_6$ sample overlap with each other. The pristine $Cs_2AgBiCl_6$ sample has the covalent bond, which is ensured by charge density distribution image. As the pressure changes, the bonding charge density increases due to the decreasing interatomic distance. The covalent bond is formed in between Bi and Ag atoms with the maximum charge density and exhibits strong electron localization.

3.3. Photo-catalytic activity

Photocatalysis is playing a key role for optoelectronic device applications. The most important parameters for efficient photocatalyst materials are considered to be narrow band gap, low recombination rate of electron-hole pair, and appropriate redox potential. The band energy diagrams of ordered and disordered $Cs_2AgBiCl_6$ are shown in Figure 7. The redox potential is measured from the states of the valence band maximum (VBM) and conduction band minimum (CBM) and the value is compared with the oxidation/reduction potential of water. Normally, a large CBM potential indicates a greater reduction power for electrons compared to the hydrogen reduction potential, while a lower VBM potential indicates a strong oxidative power for holes compared to the water oxidation potential [35].

Table 2. Mulliken effective charge of individual atoms, bond population and bond lengths of $Cs_2AgBiCl_6$ at selected pressures.

	Samples				
	0 GPa	20 GPa	40 GPa	60 GPa	80 GPa
Atoms	Mulliken effective charge (e)				
Cs	0.88	0.90	0.97	1.05	1.12
Ag	0.14	-0.22	-0.44	-0.55	-0.66
Bi	1.19	1.15	1.02	0.87	0.74
Cl	-0.52	-0.46	-0.43	-0.40	-0.39
Bond	Bond population				
Cl–Ag	0.16	0.17	0.15	0.13	0.10
Cl–Bi	0.19	0.13	0.07	0.02	-0.04
Bond	Bond length (Å)				
Cl–Ag	2.80	2.39	2.26	2.19	2.14
Cl–Bi	2.75	2.51	2.40	2.33	2.27

The theoretical position of VBM and CBM are calculated by the following Eqs. (8) and (9).

$$E_{CB} = X - E_{e-} \frac{1}{2} E_g \tag{8}$$

$$E_{VB} = E_{CB} + E_g \tag{9}$$

Here, E_{CB} and E_{VB} represent the band edge positions of CB and VB, respectively; X is the absolute electronegativity of $Cs_2AgBiCl_6$. The mean value of the electronegativity of the constituent elements is equal to the Mulliken electronegativity of the material. The initial ionization energy of an atom and the electron affinity are calculated by the Mulliken electronegativity of an atom [36]. E_e is the energy of the free electrons of hydrogen (4.5 eV) and Eg is the band gap energy.

The electronegativity (X) of $Cs_2AgBiCl_6$ is calculated 5.54 eV. The band-edge potentials of VB and CB of $Cs_2AgBiCl_6$ are shown in Figure 8 (a, b). Thermodynamically, the positive value of the momentum of $Cs_2AgBiCl_6$ ensures that the reduction of H^+ to H_2 is impposible. The CBM and VBM calculated potentials of $Cs_2AgBiCl_6$ are shown in Figure 8. VBM potentials have higher (1.97 eV) for ordered samples than O_2/H_2O (1.23 eV) and 1.37 eV for disordered samples, provide insights into the generation of O_2 from water. Furthermore, the presentation of the band-edge potentials shows the plausible reduction of H_2 and the evolution of O_2 since the redox potentials satisfy both oxidation and reduction process. As a consequence, the water splitting by $Cs_2AgBiCl_6$ is thermodynamically beneficial and the material under consideration is likely to be a good candidate for photocatalysis. Consequently, $Cs_2AgBiCl_6$ can degrade some organic pollutants and oxidize H_2O to generate H_2 and O_2 through photogenerated in the visible energy range. For optimum photocatalytic performance, the oxidation and reduction processes must be equally efficient.

The $Cs_2AgBiCl_6$ sample is highly responsive to photocatalytic properties, which is guaranteed by the redox potential. In the disordered Ag and Bi atoms belonging to the $Cs_2AgBiCl_6$ sample, the photocatalytic activity tends to increase compared with the ordered $Cs_2AgBiCl_6$ sample. The charge carrier mobility transition is one of the fundamental criteria for photocatalytic performance. In this study, the ordered $Cs_2AgBiCl_6$ shows indirect band gap, while the disordered $Cs_2AgBiCl_6$ sample shows direct band gap type. The indirect band gap belongs to ordered $Cs_2AgBiCl_6$ samples require a long time for the excitation of electron under influence of light. The disordered $Cs_2AgBiCl_6$ sample with new dopant significantly reduced the band energy. This data will be applicable to optoelectronic devices, especially solar cell applications.

3.4. Mechanical properties

To calculate the three independent elastic moduli of the cubic-structured double perovskite $Cs_2AgBiCl_6$ sample, finite strain theory was applied [37]. The elastic properties are simulated with the help of CASTEP code of material studio 8.0 and presented in Tables 3 and 4. The simulated elastic moduli of Cs2AgBiCl6 are in well matches with previous theoretical manuscript [25]. The simulated elastic constants of $Cs_2AgBiCl_6$ justified the cubic symmetry criterion under the condition of Eq. (10) [24]:

$$C_{11} + 2C_{12} > 0,\ C_{44} > 0 \text{ and } C_{11} - C_{44} > 0 \tag{10}$$

The simulated elastic constants of $Cs_2AgBiCl_6$ satisfy the mechanical stability under ambient conditions. The quantity C12–C44, is called as Cauchy pressure [38, 39], which identifies the sample mostly brittle/ductile nature. The simulated positive Cauchy pressure value ensures that both uncompressed and compressed $Cs_2AgBiCl_6$ are ductile.

The mechanical stability of the material has been studied under high pressure using the elastic stiffness coefficient, described by Eq. (11) [40].

$$B_{ijkl} = C_{ijkl} + 1/2\ [\delta_{ik}\ \sigma_{jl} + \delta_{jk}\ \sigma_{il} + \delta_{il}\ \sigma_{jk} + \delta_{jl}\ \sigma_{ik} - 2\ \delta_{kl}\ \sigma_{ij}] \tag{11}$$

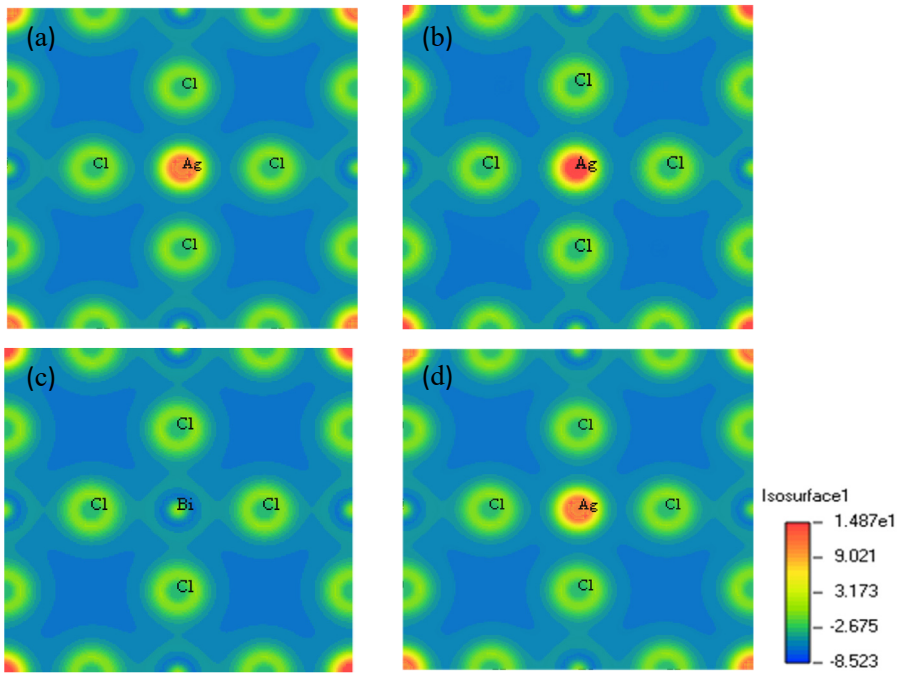

Figure 6. The electrons charge density (a) ordered, (b) disordered, and (c) 70 GPa and (d) 80 GPa of $Cs_2AgBiCl_6$.

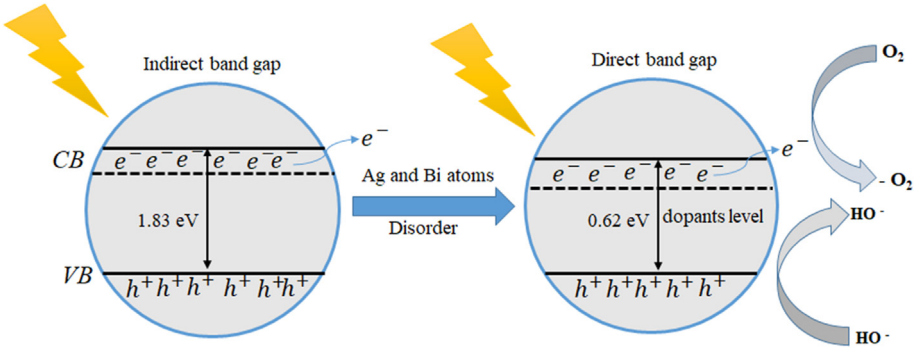

Figure 7. A schematic band energy diagram and the photocatalytic effect of the ordered and disordered $Cs_2AgBiCl_6$.

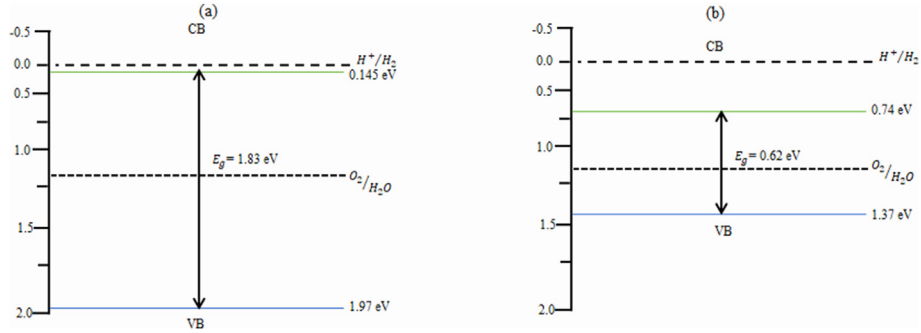

Figure 8. Potential energy diagram for the conduction band minimum and the valance band maximum of (a) ordered $Cs_2AgBiCl_6$ and (b) (Ag, Bi) disordered $Cs_2AgBiCl_6$.

Where, C_{ijk} is the elastic constant evaluated under applied stress, σ_{jl} specifies the external stress, and δ_{jk} is the Kronecker delta. Eq. (11) implies that the stiffness coefficient tensor depends on the state of the applied stress. Therefore, it has a different symmetry than the elastic constant tensor, except that it is isotropic or zero stress. Under applying the hydrostatic pressure to a cubic crystal system, the elastic stiffness coefficients are in Voigt's notation as follows: B_{ij} is $B_{11} = C_{11} - P$, $B_{12} = C_{12} + P$, $B_{44} = C_{44} - P$, where P is the hydrostatic pressure.

The calculated polycrystalline properties belong to Bulk modulus; Shear modulus, Young's modulus, Pugh's ratio and Poisson's ratio of pure and pressure induced $Cs_2AgBiCl_6$ are presented in Table 4. Bulk modulus values of the $Cs_2AgBiCl_6$ sample, indicating that the sample is flexible

Table 3. The elastic constants C_{ij} (in GPa) and Cauchy pressure of $Cs_2AgBiCl_6$ under variant pressure.

Pressure	C_{11}	C_{12}	C_{44}	C_{12}–C_{44}	Reference
0	42.42	13.65	9.25	4.44	[25]
0	41.04	11.92	7.33	4.59	This work
20	169.12	46.66	12.74	33.92	This work
40	314.05	81.98	10.67	71.31	This work
50	379.77	104.74	15.93	88.81	This work
60	434.61	121.58	13.26	108.32	This work
70	523.45	149.96	13.91	136.05	This work
80	560.85	157.75	14.86	142.89	This work

Table 4. The mechanical parameters of $Cs_2AgBiCl_6$ under variant pressure.

Pressure	B (GPa)	G (GPa)	Y (GPa)	B/G	ν	Reference
0	23.20	11.27	35.62	2.06	0.24	[25]
0	28.09	10.23	19.89	2.74	0.27	This work
20	87.48	32.13	85.89	2.72	0.33	This work
40	159.34	52.81	124.12	3.01	0.35	This work
50	196.41	64.56	174.57	3.04	0.35	This work
60	226.59	70.96	192.76	3.19	0.35	This work
70	274.46	83.04	226.31	3.32	0.36	This work
80	292.12	89.54	243.74	3.26	0.36	This work

and soft. Pugh's ratio (Bulk to Shear modulus) and Poisson's ratio can identify the ductility or the brittle nature of a material [41, 42, 43, 44]. The pressure dependent elastic constant C_{ij} and elastic stiffness coefficient B_{ij} in $Cs_2AgBiCl_6$ is shown in Figure 9. The elastic constants C_{11}, C_{12} and C_{44} increase with increasing hydrostatic pressure. The same happens with B11 and B12 increase, but B44 decreases with pressure reaching negative values beyond 10 GPa. This suggests that the crystal structure becomes mechanical unstable, and a phase transition could be induced by pressure [45]. The bulk modulus of 23–28 GPa makes the studied compounds as compressible as metal-organic frameworks [46]. The critical value of Pugh's and Poisons determines the brittleness from ductile ones. If the Pugh's (1.75) and Poisson's ratio (0.26) values are higher than critical values, then the sample is said to be in ductile types, otherwise, brittle types. The Pugh's and Poisson's values ensured that pure and pressure induced $Cs_2AgBiCl_6$ samples have ductile natures. The mechanical properties indicate that the $Cs_2AgBiCl_6$ sample is suitable for the thin film industry.

3.5. Optical properties

To comprehend the optical properties, the optical absorption (α), electrical conductivity (σ) and permittivity (ε) of pure and pressure-induced $Cs_2AgBiCl_6$ are measured. The dielectric function is determined by Eq. (12) [47].

$$\varepsilon(\omega) = \varepsilon_1(\omega) + i\varepsilon_2(\omega) = N^2 \tag{12}$$

Where, ε_1 (ω) and $i\,\varepsilon_2$ (ω) refers to the real and imaginary part of the complex dielectric constant as a function frequency (ω). N represents the complex refractive index. The imaginary dielectric function is described by Eq. (13) [48].

$$\varepsilon_2 = \frac{2\pi e^2}{\Omega\varepsilon_0} \sum_{k,\,v,\,c} \left[\Psi_k^c\right] \boldsymbol{u}.\boldsymbol{r} \left[\Psi_k^c\right]^2 \delta\left(E_k^c - E_k^v - E\right) \tag{13}$$

Where, e, Ω, and u represent the electron charge, unit cell volume, and unit volume, respectively.

In order to see the optical properties, photon energies (E) are considered in between 0 to 20 eV. Herein, a Gaussian tail of 0.5 eV was taken. The calculation of optical properties was performed on the {100} plane. The scissor value was set at 0.25 eV to calculate the light absorption and dielectric function. The calculated values of real and imaginary parts of the optical conductivity and the dielectric function are clearly shown in Fig.10 (a-f).

The first absorption peak is expected to be around 3.95 eV, the most significant value for device applications. It is observed that in the visible and ultraviolet-regions, $Cs_2AgBiCl_6$ sample have a strong absorption. But the pressure-driven $Cs_2AgBiCl_6$ perovskite has a strong optical absorption in the ultraviolet region in compared with pure sample. The absorption spectra are transferred from blue-shift into redshift with a strong absorption edge at around 130 nm.

The optical absorption of $Cs_2AgBiCl_6$ strongly related to the electronic structure of the material. It is well known that the stronger light-absorbing samples are suitable for photovoltaic applications. Optical conductivity (1/fs) of the sample shows the response of the electromagnetic signal [48]. When a sample is subjected to an electric field, it exhibits electrical conductivity and relates the current density at its natural frequency. The optical and electrical conduction is achieved under the response of photon absorption and the escape of electron in the higher states. It is observed that the real part disappears at around 10.5 eV, indicates an optical anisotropic nature of $Cs_2AgBiCl_6$. The $Cs_2AgBiCl_6$ sample escapes free carriers in the conduction band under absorbing energy. To calculate the level of electromagnetic radiation response in the material, the complex dielectric function [49] was used. Electron excitation is represented by the imaginary part (ε_2) of the dielectric function. Owing to the intra-band transitions inside the Bi 6p and Ag 3d orbital, the first peak of the imaginary part of the dielectric function (ε_2) is predicated more or less at < 1.5 eV. The consideration of the frequency limit tends to zero ε1 (0) is the essential part of the dielectric constant measurement. The real part of the permittivity of the pressure driven $Cs_2AgBiCl_6$ starts to rise from zero frequency and reaches its maximum peak. Then it starts to militate and undergoes below zero by releasing energy. Hence, the incident photon beam is totally attenuated [50]. A comprehensive data on the optical properties of pure and pressure-induced $Cs_2AgBiCl_6$ samples may be applicable to photocatalytic applications.

4. Conclusion

Briefly, the structure, stability of phase, mechanical, optical, electronic properties and photocatalytic activity of pure and pressure-induced $Cs_2AgBiCl_6$ dihalide perovskites were investigated by DFT method. The lattice constant (a) and the unit cell volume (V) decreases with increasing driving pressure. The dynamic stability was confirmed by the phonon dispersion models. The heat capacity at high temperature indicates that the pressure-driven samples are thermally stable. The disorder of Ag^{+}/Bi^{3+} cations in its sub-lattice creates antisite defects, which are important for optoelectronic device applications. In disordered $Cs_2AgBiCl_6$, the Bi 6p and Ag 3d orbitals significantly change the conduction band due to the shift of the R and Γ k points. In this case, the bandgap energy is transformed indirect to direct, and the band gap energy is significantly reduced. The anti-site defect in the sub lattice of $Cs_2AgBiCl_6$, opens a new avenue for optoelectronic and photovoltaic material design. It is observed that the pressure-induced samples have transformed from semiconductor to metal. Pressure-driven samples in $[AgBi]^{-6}$ and $[AgCl]^{-6}$ octahedral sites due to conduction and valence band overlap with each other's. The bond lengths, Ag–Bi and Bi–Cl reduce the driving pressure due to crystal defects in the Ag and Bi lattice networks. Mechanical properties show that unpressured and pressured actuation $Cs_2AgBiCl_6$ samples are mechanically stable. The data of Pugh's and Poisson's ratio's favors the pure and pressure driven $Cs_2AgBiCl_6$ for applications in the film coating industry. The absorption edge moves (redshift) toward the lower energy region under induced pressure. Phase-

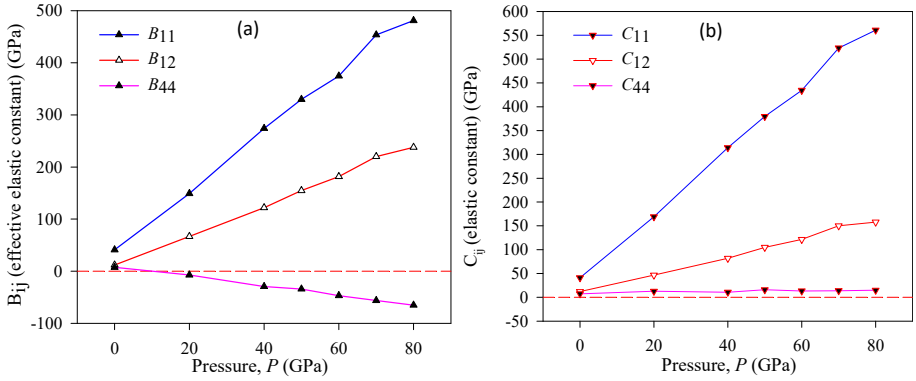

Figure 9. Pressure dependence of (a) elastic stiffness coefficient (B_{ij}) and (b) elastic constant (C_{ij}) of $Cs_2AgBiCl_6$.

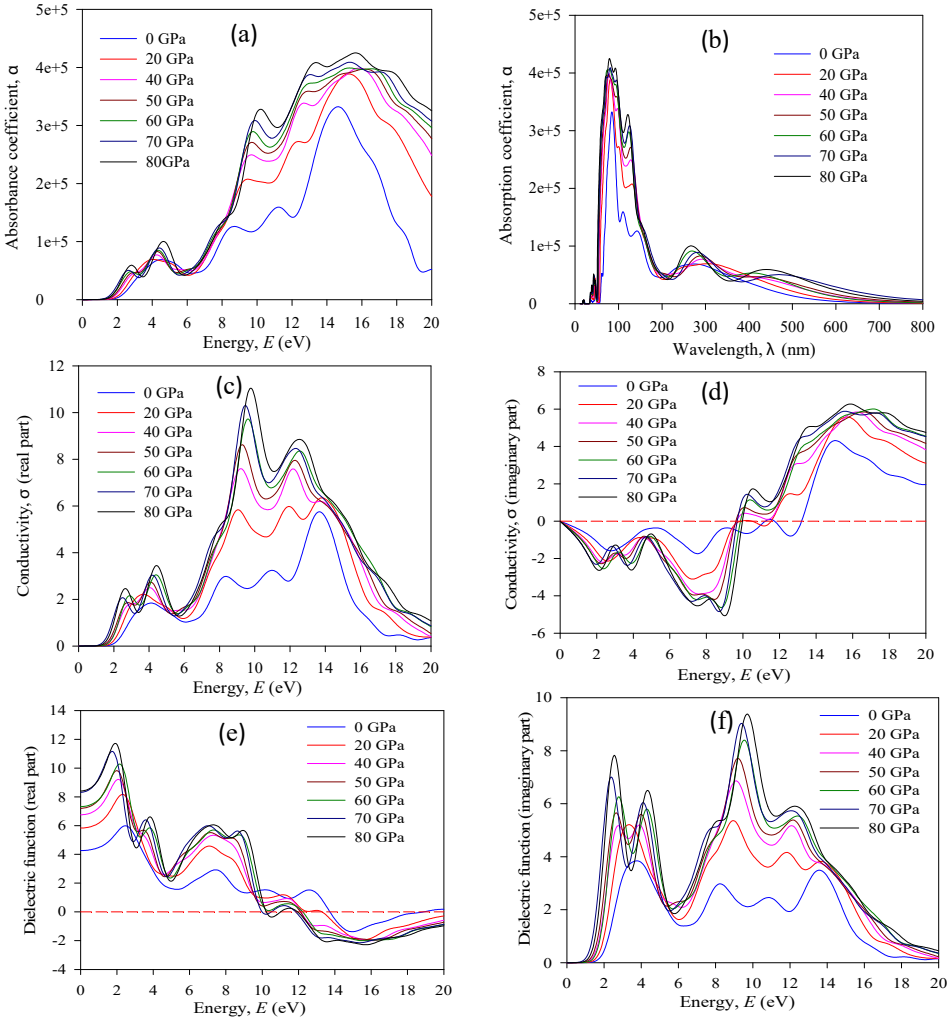

Figure 10. The calculated optical properties: (a) absorbance vs. energy, (b) absorbance vs. wavelength, (c) conductivity (real part), (d) conductivity (imaginary part), (e) real dielectric function, (f) imaginary dielectric function of the pressure-driven $Cs_2AgBiCl_6$ samples.

change lead-free double halide materials have obtained a variety of outstanding properties, providing a broad space for industrial applications. The overall investigation suggests that pure and pressure-driven $Cs_2AgBiCl_6$ samples may be well suited for photovoltaic and optoelectronics, especially solar cells. It is expected that this first-principles simulation study will provide a better understanding of band structure calculations and motivate to the experimental investigations.

Declarations

Author contribution statement

Md. Nurul Islam: Conceived and designed the experiments; Performed the experiments; Analyzed and interpreted the data; Wrote the paper.

Jiban Podder: Conceived and designed the experiments; Analyzed and interpreted the data; Contributed reagents, materials, analysis tools or data.

Funding statement

This research did not receive any specific grant from funding agencies in the public, commercial, or not-for-profit sectors.

Data availability statement

Data will be made available on request.

Declaration of interests statement

The authors declare no conflict of interest.

Additional information

No additional information is available for this paper.

Acknowledgements

The authors are thankful to the spray pyrolysis and the crystal growth laboratory of the Department of Physics, Bangladesh University of Engineering and Technology, Dhaka, Bangladesh for performing this theoretical research using the laboratory computer facilities and software.

References

[1] H. Zhou, Q. Chen, G. Li, S. Luo, T.B. Song, H.S. Duan, Z. Hong, J. You, Y. Yang, Interface engineering of highly efficient perovskite solar cell, Science 345 (2014) 542–546.
[2] J. Burschka, N. Pellet, S.-J. Moon, R. Humphry-Baker, P. Gao, M.K. Nazeeruddin, M. Grätzel, Sequential deposition as a route to high-performance perovskite-sensitized solar cells, Nature 499 (2013) 316–319.
[3] A.B. Wong, M. Lai, S.W. Eaton, Y. Yu, E. Lin, L. Dou, A. Fu, P. Yang, Growth and anion exchange conversion of $CH_3NH_3PbX_3$ nanorod arrays for light-emitting diodes, Nano Lett. 15 (2015) 5519–5524.
[4] Y. Fu, H. Zhu, A.W. Schrader, D. Liang, Q. Ding, P. Joshi, L. Hwang, X.-Y. Zhu, S. Jin, Nanowire lasers of formamidinium lead halide perovskites and their stabilized alloys with improved stability, Nano Lett. 16 (2016) 1000–1008.
[5] E. Zheng, B. Yuh, G.A. Tosado, Q. Yu, Solution processed visible-blind UV-A photo detectors based on $CH_3NH_3PbCl_3$ perovskite thin films, J. Mater. Chem. C 5 (2017) 3796–3806.
[6] J.S. Manser, M.I. Saidaminov, J.A. Christians, O.M. Bakr, P.V. Kamat, Making and breaking of lead-halide perovskites, Acc. Chem. Res. 49 (2016) 330–338.
[7] K. Dave, M.H. Fang, Z. Bao, H.T. Fu, R.S. Liu, Recent developments in lead-free double perovskites: structure, doping, and applications, Chem. Asian J. 15 (2020) 242–252.
[8] A.H. Slavney, B.A. Connor, L. Leppert, H.I. Karunadasa, A pencil-and-paper method for elucidating halide double perovskite band structures, Chem. Sci. 10 (2019) 11041–110453.
[9] J. Yang, P. Zhang, S.H. Wei, Band structure engineering of $Cs_2AgBiBr_6$ perovskite through order–disordered, J. Phys. Chem. Lett. 9 (2017) 31–35.
[10] C. Han, G. Ji, S. Hu, R. Mi, P. Fu, K.Z. Du, Z. Xiao, B-site columnar-ordered halide double perovskites $A_2B(II)'$ $0.5B(II)X_5$ with $B(II)'$/Vacancy disordering, Chem. Mater. 17 (2021) 7106–7112.
[11] X. Ma, Z. Li, J. Yang, Efficient direct band gap photovoltaic material predicated via doping double halide perovskites Cs_2AgBiX_6 (X= Br, Cl), J. Phys. Chem. C 125 (2021) 10868–10875.
[12] Y. Liang, X. Huang, Y. Huang, X. Wang, F. Li, Y. Wang, F. Tian, B. Liu, Z.X. Shen, T. Cui, New metallic ordered phase of perovskite $CsPbI_3$ under pressure, Adv. Sci. 6 (2019), 1900399.
[13] T. Yin, B. Liu, J. Yan, Y. Fang, M. Chen, W.K. Chong, S. Jiang, J.L. Kuo, J. Fang, P. Liang, S. Wei, Pressure-engineered structural and optical properties of two-dimensional $(C_4H_9NH_3)_2PbI_4$ perovskite exfoliated nm-thin flakes, J. Am. Chem. Soc. 141 (2018) 1235–1241.
[14] Z. Ma, Z. Liu, S. Lu, L. Wang, X. Feng, D. Yang, K. Wang, G. Xiao, L. Zhang, S.A. Redfern, B. Zou, Pressure induced emission of cesium lead halide perovskite nanocrystals, Nat. Commun. 9 (2018) 1–8.
[15] L. Wang, P. Yao, F. Wang, S. Li, Y. Chen, T. Xia, E. Guo, K. Wang, B. Zou, H. Guo, Pressure-induced structural evolution and bandgap optimization of lead-free halide double perovskite $(NH_4)_2SeBr_6$, Adv. Sci. 7 (2020), 1902900.
[16] M.N. Islam, J. Podder, T. Saha, P. Rani, Semiconductor to metallic transition under induced pressure in $Cs_2AgBiBr_6$ double halide perovskite: a theoretical DFT study for photovoltaic and optoelectronic applications, RSC Adv. 11 (2021), 24001.
[17] M.A. Hadi, R.V. Vouk, A. Chroneos, Physical properties of the recently discovered Zr_2 $(Al_{1-x}$ $Bi_x)$ C MAX phases, J. Mater. Sci. Mater. Electron. 27 (2017), 11925.
[18] M.N. Islam, J. Podder, The role of Al and Co co-doping on the band gap tuning of TiO_2 thin films for applications in photovoltaic and optoelectronic devices, Mater. Sci. Semicond. Process. 121 (2021), 105419.
[19] M. Babu, C.B. Dev, J. Podder, N. Islam, Influence of Fe^{2+}/Fe^{3+} ions in tuning the optical band gap of SnO_2 nanoparticles synthesized by TSP method: surface morphology, structural and optical studies, Mater. Sci. Semicond. Process. 89 (2019) 223.
[20] C. Li, X. Lu, W. Ding, L. Feng, Y. Gao, Z. Guo, Formability of abx_3 (x= f, cl, br, i) halide perovskites, Acta Crystallogr. 64 (2008) 702.
[21] S.J. Clark, M.D. Segall, C.J. Pickard, P.J. Hasnip, M.I. Probert, K. Refson, M.C. Payne, First principles methods using CASTEP, Z. Kristallogr. 220 (2005) 567–570.
[22] M.A. Hadi, M. Dahlqvist, S.R. Christopoulos, S.H. Naqib, A. Chroneos, A.K.M.A. Islam, Chemically stable new MAX phase V_2SnC: a damage and radiation tolerant TBC material, RSC Adv. 10 (2020) 43783–43798.
[23] C. Lan, S. Zhao, J. Luo, P. Fan, First-principles study of anion diffusion in lead-free halide double perovskites, Phys. Chem. Chem. Phys. 20 (2018) 24339–24344.
[24] M.A. Hadi, M.N. Islam, M.H. Babu, Cubic perovskite Pb(Mg1/3Nb2/3)O3: a damage tolerant, machinable, and thermal barrier coating material, Z. Naturforsch. 74 (2019) 71–81.
[25] M.N. Tripathi, A. Saha, S. Singh, Structural, elastic, electronic and optical properties of lead-free halide double perovskite Cs_2AgBiX_6 (X = Cl, Br, and I), Mater. Res. Express 6 (2019), 115517.
[26] L. Zhang, Y. Fang, L. Sui, J. Yan, K. Wang, K. Yuan, W.L. Mao, B. Zou, Tuning emission and Electron−Phonon coupling in lead-free halide double perovskite $Cs_2AgBiCl_6$ under pressure, ACS Energy Lett. 4 (2019) 2975–2982.
[27] B. Luo, X. Wang, E.T.G. Lic, L. Li, Electronic structure, optical and dielectric properties of $BaTiO_3/CaTiO_3/SrTiO_3$ ferroelectric superlattices from first-principles calculations, J. Mater. Chem. C 3 (2015) 8625–8633.
[28] M.N. Islam, M.A. Hadi, J. Podder, Influence of Ni doping in a lead-halide and a lead-free halide perovskite for optoelectronic applications, AIP Adv. 12 (2019), 125321.
[29] Lotfi Ibrahim Karaouzène, Tarik Ouahrani, Ángel Morales-García, Daniel Errandonea, Theoretical calculations of the effect of nitrogen substitution on the structural, vibrational, and electronic properties of wolframite-type ScTaO4 at ambient conditions, Dalton Trans. 51 (2022) 3642–3651.
[30] L. Zhang, Y. Fang, L. Sui, J. Yan, K. Wang, K. Yuan, W.L. Mao, B. Zou, Tuning emission and electron-phonon coupling in lead-free halide double perovskites $Cs_2AgBiCl_6$ under pressure, ACS Energy Lett. 4 (2019) 2975–2982.
[31] R.S. Lamba, P. Basera, S. Bhattacharya, S. Sapra, Band gap engineering in Cs_2 $(Na_x$ $Ag_{1-x})$ $BiCl_6$ double perovskite nanocrystals, J. Phys. Chem. Lett. 10 (2019) 5173–5181.
[32] R.S. Mulliken, Electronic population analysis on LCAO-MO molecular wave functions, I. J Chem Phys. 23 (1955) 1833–1840.
[33] M.D. Segall, R. Shah, C.J. Pickard, M.C. Payne, Population analysis of plane-wave electronic structure calculations of bulk materials, Phys. Rev. B 54 (1996), 16317.
[34] D. Errandonea, D. Martínez-García, A. Segura, J. Haines, E. Machado-Charry, E. Canadell, J.C. Chervin, A. Chevy, High-pressure electronic structure and phase transitions in monoclinic InSe: X-ray diffraction, Raman spectroscopy, and density functional theory, Phys. Rev. B 77 (2008), 045208.
[35] M. Roknuzzaman, J.A. Alarco, H. Wang, A. Du, T. Fesfamichael, K. Ostrikov, Ab initio atomistic insights into lead-free formamidinium based hybride perovskites for photovoltaic and optoelectronics, Comput. Mater. Sci. 169 (2019), 109118.
[36] H. Tang, K. Prasad, R. Sanjines, P. Schmid, F. Levy, Electrical and optical properties of TiO_2 anatase thin films, J. Appl. Phys. B. 75 (1994) 2042–2047.
[37] D. Liyuan, S. Shijing, D. Zeyu, L. Wei, W. Fengxia, Q. Yajun, L. Yanchun, L. Xiaodong, L. Peixiang, U. Ramanurty, Elastic properties and thermal expansion of lead-free halide double perovskite $Cs_2AgBiBr_6$, Comput. Mater. Sci. 141 (2018) 49–58.
[38] D.G. Pettifor, Theoretical predictions of structure and related properties of intermetallics, Mater. Sci. Technol. 8 (1992) 345–349.
[39] Y. Weinan, N. Guangda, X. Yeming, W. Haodi, W. Huamin, Y. Hang, L. Peng, L. Wenzhe, F. Jiandong, In situ regulating the order–disorder phase transition in $Cs_2AgBiBr_6$ single crystal toward the application in an X-ray detector, Adv. Funct. Mater. 29 (2019), 1900234.
[40] O. Gomis, B. Lavina, P.R. Hemandez, A. Munoz, R. Errandonea, D. Errandonea, M. Bettinelli, High-pressure structural, elastic, and thermodynamic properties of zircon-type HoPO4 and TmPO4, J. Phys. Condens. Matter 29 (2017), 095401.
[41] L. Chunfeng, Z. Shuai, L. Jingting, F. Ping, First-principles study of anion diffusion 1in lead-free halide double perovskites, Phys. Chem. Chem. Phys. 20 (2018), 24344.
[42] Z. Jun, X. Zhiguo, M.S. Maxim, Z. Xiuwen, P. Dongsheng, L. Quanlin, Composition design, optical gap and stability investigations of lead-free halide double perovskite Cs_2 $AgInCl_6$, J. Mater. Chem. 5 (2017), 15037.
[43] S. Bouguima, T. Ouahrani, A. Bouheddadj, M.L. Roux, D. Errandonea, M. Badawi, Understanding the optical and bonding properties of hybrid metal-halide (C_5H1_6NP) PbX_4 (X = Cl, Br, I) perovskite: a density-functional theory study, Inorg. Chem. Commun. 130 (2021), 108721.
[44] M.N. Islam, J. Podder, M.L. Ali, The effect of metal substitution in $CsSnI_3$ perovskites with enhanced optoelectronic and photovoltaic properties, RSC Adv. 11 (2021), 39553.

[45] A.B. Garg, D. Errandonea, P. Rodríguez-Hernández, A. Muñoz, High-pressure monoclinic–monoclinic transition in fergusonite-type $HoNbO_4$, J. Phys. Condens. Matter 33 (2021), 195401.
[46] José Navarro-Sánchez, Ismael Mullor-Ruíz, Catalin Popescu, David Santamaría-Pérez, Alfredo Segura, Daniel Errandonea, Javier González-Platas, Carlos Martí-Gastaldo, Peptide metal–organic frameworks under pressure: flexible linkers for cooperative compression, Dalton Trans. 47 (2018) 10654–10659.
[47] K.O. Obodo, G. Gebreyesus, C.N.M. Ouma, J.T. Obod, S.O. Ezeonu, D.P. Raif, B. Bouhafs, Controlling the electronic and optical properties of HfS_2 mono-layers via lanthanide substitutional doping: a DFT+ U study, RSC Adv. 10 (2020), 15670.
[48] M.A. Hadi, Md Roknuzzaman, M.T. Nasir, U. Monira, S.H. Naqib, A. Chroneos, A.K.M.A. Islam, Jose A. Alarco, Kostya (ken) Ostrikov, effects of Al substitution by Si in Ti_3AlC_2 nanolaminate, Sci. Rep. 11 (2021) 3410.
[49] H. Ayatullahah, G. Murtaza, S. Muhammad, S. Naeem, M.N. Khalid, A. Manzar, Physical properties of $CsSnM_3$ (M ¼ Cl, Br, I): a first principle study, Acta Phys. Pol., A 124 (2013) 102–107.
[50] X. Liu, B. Xie, C. Duan, Z. Wang, B. Fan, K. Zhang, B. Lin, F.J. Colberts, W. Ma, R.A. Janssen, F. Huang, A high dielectric constant non-fullerene acceptor for efficient bulk-heterojunction organic solar cells, J. Mater. Chem. 6 (2018) 395–403.